MRS Communications (2018), 1 of 9

doi:10.1557/mrc.2018.117

MRS Communications

Research Letter

Structural, optical, and hole transport properties of earth-abundant chalcopyrite ($CuFeS_2$) nanocrystals

Ebin Bastola, Khagendra P. Bhandari, Indra Subedi, Nikolas J. Podraza, and **Randy J. Ellingson,** Department of Physics and Astronomy, The Wright Center for Photovoltaics Innovation and Commercialization (PVIC), University of Toledo, Toledo, Ohio 43606, USA

Address all correspondence to Randy J. Ellingson at **Randy.Ellingson@utoledo.edu**

(Received 18 April 2018; accepted 19 June 2018)

Abstract

Here, we report thiol-free thermal-injection synthesis of chalcopyrite ($CuFeS_2$) nanocrystals (NCs) using iron (II) bromide ($FeBr_2$), copper (II) acetaylacetonate ($Cu(acac)_2$), and elemental sulfur (S). Controlled reaction temperature and growth time yield stable and phase-pure ternary $CuFeS_2$ NCs exhibiting tetragonal crystal structure. With increasing growth time from 1 to 30 min, absorption peak slightly red shifts from 465 to 490 nm. Based on spectroscopic ellipsometry analysis, three electronic transitions at 0.652, 1.54, and 2.29 eV were found for $CuFeS_2$ NC film. Also, $CuFeS_2$ NC thin films are incorporated as hole transport layers in cadmium telluride solar cells reaching an efficiency of ~12%.

Introduction

Chalcopyrite materials have attracted special attention in the field of opto-electronic applications due to their abundance, and low toxicity composition compared with other semiconducting materials. Semiconducting bulk chalcopyrite, $CuFeS_2$, exhibits an indirect band gap of ~0.5–0.6 eV and tetragonal crystal structure,[1] in which Cu and Fe ions bond tetrahedrally with sulfur (S).[2] Recent publications indicate that this chalcopyrite is promising for thermoelectric applications due primarily to low resistivity and thermal conductivity.[3,4] Additionally, these narrow gap semiconductors are suitable for the development of counter electrodes,[5] infrared (IR) detectors, and light-to-heat converters.[6] Colloidal nanocrystals (NCs) of the $CuFeS_2$ chalcopyrite materials are being investigated to exploit their unique properties such as quantum confinement, solution-processability, and facile synthesis methods. However, development and application of ternary and quaternary colloidal NCs have been challenging due to the required control over phase purity and the stability of the synthesized NC materials.[7] To make the material more device applicable, research has demonstrated various techniques for the fabrication of $CuFeS_2$ chalcopyrite.

The common solution-based syntheses employed to prepare $CuFeS_2$ chalcopyrite nanostructures are solvothermal[8] and hydrothermal[9] methods. In addition, a mechanical alloying preparation method has also been reported for $CuFeS_2$ materials.[4,10] Wang et al. have synthesized shape-controlled $CuFeS_2$ NCs with spherical and pyramidal morphology using a solution-based method, and have reported blue shifting features within the absorption spectrum for quantum-confined spherical $CuFeS_2$ NCs as compared with their bulk counterpart.[11] Kumar et al. have reported solution-based single step synthesis of polymorphs of $CuFeS_2$ NCs using Cu(I) thiourea complex with $Fe_2(SO_4)_3$ and $FeCl_3$ separately in ethylene glycol,[12] however, they have not reported the electronic properties such as resistivity, carrier concentration, or mobility of these $CuFeS_2$ chalcopyrite NCs. Investigation of the electronic properties allows for consideration of appropriate applications of these NCs in opto-electronic devices. Liang et al. have demonstrated that solution-synthesized $CuFeS_2$ material exhibits ~77 times larger thermoelectric figure of merit (ZT) value compared with the bulk $CuFeS_2$ chalcopyrite.[3] As an alternative approach, Gabka et al. attempted to synthesize $CuFeS_2$ NCs by injecting S-oleyalmine complex using the hot-injection method, but they were unsuccessful.[13] Hot-injection is a common route for the synthesis of pure and composition-controlled alloyed iron pyrite NCs.[14,15] Very few publications are available pertaining to the hot-injection synthesis of $CuFeS_2$ NCs.[6,16] Previously, Ghosh et al. used only dodecanthiol (DDT) as the S source while Bhattacharyya et al. used DDT together with elemental sulfur powder as the S source.[6,16] It should be noted that DDT is a toxic compound compared with elemental S powder. Another recent publication shows an application of colloidal $CuFeS_2$ NCs as the counter electrodes in dye-sensitized solar cells.[5] However, synthesis of phase pure $CuFeS_2$ NCs using elemental sulfur powder as the S source is difficult due to the low reactivity of elemental S compared with other S sources such as DDT and bis (trimethylsilyl) sulfide ($(tms)_2S$).

Colloidal NCs have wide-ranging applications in opto-electronics including photovoltaic (PV) absorbing layers or contact layers. Previously, solution-processed iron pyrite

(FeS_2) NC-based thin films have been successfully applied as the hole transport layers (HTLs) in cadmium telluride (CdTe) and perovskite solar cells (PKSCs).[17–20] The ideal HTLs for CdTe solar cells have high carrier concentration ($\geq 10^{18}$ cm^{-3}) and deep valence band (VB) level to match with CdTe to reduce overall contact resistance.[21]

The apparent band gap of bulk chalcopyrite $CuFeS_2$ (~0.6 eV)[1] is small compared with other chalcopyrite semiconductors such as $CuAlS_2$ (3.5 eV)[22] and $CuGaS_2$ (2.5 eV)[22]. The study of opto-electronic properties shows that chalcopyrite $CuFeS_2$ materials exhibit two intermediate bands (assigned as IB I and IB II), predominantly formed by vacant Fe 3d orbitals between the VB and the conduction band (CB).[6,23] The mid-gap absorption is strong in the case of $CuFeS_2$ due to the electronic transition from VB to the IB.[23,24] Experimental studies of the absorption spectra of single crystal and thin film polycrystalline $CuFeS_2$ have revealed three strong absorption bands at approximate photon energies of 1.0 eV (VB to IB I), 2.1 eV (VB to IB II), and 3.2 eV (VB to CB), in accord with theoretical predictions.[23,24]

The electronic properties of $CuFeS_2$ NCs indicate that these materials could be applied as the HTLs in energy harvesting applications. At the laboratory scale, Cu/Au is commonly used as a standard back contact in CdS/CdTe solar cells.[25] However, an HTL layer is desired in CdTe solar cells to improve transport of the photogenerated holes because CdTe's deep VB edge (~−5.9 eV)[21] and work function (~5.4–5.7 eV) render an ohmic contact elusive. Instead, a Schottkey barrier forms at the interface between CdTe and Au (work function of Au is ~5.0 eV), and the presence of Cu narrows the barrier to facilitate hole transfer across. Any hole transport material applied to CdTe PV should be earth-abundant and of low toxicity to minimize the environmental impact and cost ($/Watt) of the solar cells, and hence the researchers are investigating the possible applications of earth-abundant materials as HTLs in energy harvesting applications. Further, the researchers have been exploring other materials to replace elemental Cu to prevent potential diffusion and degradation of the solar cells over a long period of time.

Here, we report the analysis of colloidal $CuFeS_2$ NCs prepared by thermal injection synthesis based on iron (II) bromide ($FeBr_2$), copper (II) acetylacetonate ($Cu(acac)_2$), and elemental S powder (Scheme 1). The synthesized $CuFeS_2$ NCs are characterized by X-ray diffraction (XRD), electron microscopy, Raman spectroscopy, and near IR to ultraviolet spectral range unpolarized transmittance. The $CuFeS_2$ NCs grown by injecting S precursor at 240 °C are phase-pure, exhibiting tetragonal crystal structure in chalcopyrite phase with consistent elemental composition as confirmed by elemental energy dispersive X-ray spectroscopy (EDS) mapping and analysis. The temperature and time-dependence growth of these $CuFeS_2$ NCs have been studied. Three electronic transitions at 0.652, 1.54, and 2.29 eV for $CuFeS_2$ NC films are identified from the complex optical property spectra obtained by analysis of spectroscopic ellipsometry measurements. Additionally, the preliminary test of NC thin films as HTLs in CdTe solar cells shows promising results with the best device efficiency reaching ~12%.

Experimental section

The chalcopyrite ($CuFeS_2$) NCs were synthesized using a modified procedure reported previously for iron dichalcogonides NCs.[14,26] In a typical synthesis, 0.25 mmol (53 mg) iron (II) bromide, 0.25 mmol (65 mg) copper acetylacetonate $Cu(acac)_2$, 3 mmol (1.16 g) TOPO, and 10 mL oleylamine (OLA) were taken in a three-neck flask, evacuated for about 30 min at 120 °C, and then the flask temperature was maintained at 170 °C for about 3 h in nitrogen environment using a standard Schlenk line system. The S precursor was prepared by dissolving 3 mmol (96 mg) elemental S powder in 5 mL OLA with sonication for ~15 min. The S precursor solution was injected into the three-neck flask at an elevated temperature ≥170 °C, and the NCs were grown for a different time under nitrogen environment. The reaction was quenched by removing the heating mantle, and the flask was allowed to cool down to the room temperature. The synthesized NCs were cleaned using standard suspension and precipitation method with chloroform and methanol 3 times. The NCs so obtained were stored in a glove box for further characterization. Further, nanocrystalline thin films were prepared using layer-by-layer drop-casting/spin-coating onto a soda lime glass substrate for characterization. For this, $CuFeS_2$ NC solution was prepared in chloroform at a concentration of ~8 mg/mL. The detail of characterization and photovoltaic device fabrication are included in supporting information (SI).

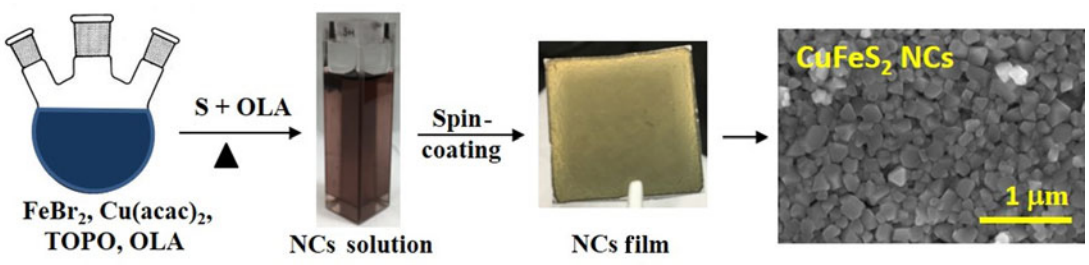

Scheme 1. Thiol-free Synthesis and Film Fabrication of Chalcopyrite ($CuFeS_2$) Nanocrystals.

Results and discussion

Phase analysis and surface morphology

Phase structures of the $CuFeS_2$ NCs were identified from XRD patterns as shown in Fig. 1. Initially, we started growing these NCs using a procedure identical to that used to prepare FeS_2 NCs.[14] The S precursor was injected into the reaction flask containing Fe and Cu ions at 220 °C, and the NCs were allowed to grow at the same temperature for about 2 h. The XRD pattern of these NCs revealed additional peaks, marked by * and ** in Fig. 1, attributed to other phase materials in addition to the peaks of $CuFeS_2$. The peak marked by * at 27.7° is assigned to covellite (CuS) particles produced during the synthesis of $CuFeS_2$ NCs. The CuS peak is assigned based on the chemical composition and its diffraction pattern being close to the standard pattern of $CuFeS_2$. Similarly, the peak marked by ** is assigned to mackinawite (FeS) crystallites. The covellite particle has hexagonal crystal structure while mackinawite has a tetragonal crystal structure.[27,28] The additional XRD peaks such as at 27.7° were observed when the S injection and growth temperatures were ≤240 °C. These additional peaks observed in the XRD pattern prevent the synthesis of phase pure $CuFeS_2$ NCs using elemental S powder. Ultimately, the phase pure $CuFeS_2$ NCs were synthesized when the S precursor was injected at 240 °C, and the NCs were grown at an elevated temperature of 270 °C for about 2 h. As the S precursor was injected at 240 °C, the temperature of reaction solution dropped to ~205 °C, and the temperature was immediately set to growth temperature 270 °C. This S injection and growth temperature produced phase pure NCs based on the XRD pattern which showed no discernible other phases or compositions. This statement regarding the phase purity of the synthesized NCs is supported by the intense and sharp peaks of the XRD pattern of $CuFeS_2$ NCs presented in Fig. 1. These phase pure $CuFeS_2$ NCs belong to tetragonal chalcopyrite phase with the XRD pattern matching exactly with the standard expectation for tetragonal $CuFeS_2$ chalcopyrite material (#PDF 98-000-0156) (space group, $I\bar{4}2d$) obtained from MDI JADE (Jade™ computer software from Materials Data Inc.). Based on our observation, when the injection and growth temperatures ≤240 °C, it is favorable to the formation of $CuFeS_2$ NCs in addition to some traces of impurities. During the synthesis, the mole fraction for the elemental S powder was 6 times larger than the metal (Cu and Fe) sources which are essential to obtain the phase pure $CuFeS_2$ NCs. This result agrees excellently with the XRD pattern of $CuFeS_2$ material synthesized by solution-based and mechanical alloying method reported previously.[10–12] In the tetragonal crystal system, the lattice parameters are $a = b = 0.5289$ nm, $c = 0.1042$ nm with all the three angles equal to 90°.[7]

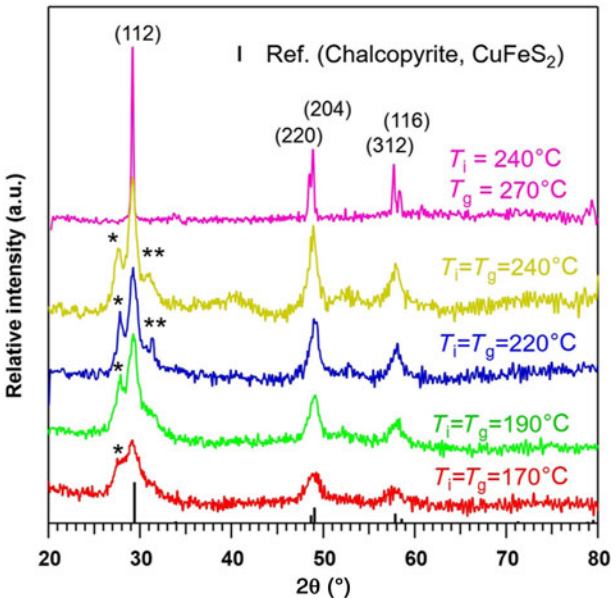

Figure 1. x-ray diffraction (XRD) patterns of as-synthesized $CuFeS_2$ nanocrystals (NCs) at various injection (T_i) and growth (T_g) temperatures. The XRD pattern matches well with the standard pattern of chalcopyrite ($CuFeS_2$) obtained from MDI JADE software (#PDF 98-000-0156), confirming this material is tetragonal $CuFeS_2$ chalcopyrite NCs.

The structure of $CuFeS_2$ NCs synthesized by S precursor injection at 240 °C and grown at 270 °C for 5, 10, 15, 30, and 60 min are characterized by XRD patterns shown in Fig. S1. Here, we note that all the synthesis temperatures other than 270 °C were for 2 h. Based on these XRD patterns, NC batches grown longer than 10 min are phase pure tetragonal $CuFeS_2$ NCs. For NCs with a growth time of 5 min, the products include a measurable quantity of covellite (CuS) particles as indicated by the small peak observed at ~27.7°; note that this XRD feature is similar to that observed for NCs in which the S precursor was injected at ≤240 °C. When the S precursor was injected, the reaction mixture temperature dropped to ~205 °C, and this temperature produced traces of covellite CuS in addition to $CuFeS_2$. Based on the literature, 205 °C supports the formation of CuS particles[27,29] and the reaction mixture took ~5 min to reach 270° C. However, the evolution of the XRD pattern with growth time shows that the diffraction peak at ~27.7° disappeared, within the limit of XRD measurement, indicating that the impure phase particles such as CuS reacted with Fe/S complexes in the excess S environment to form the phase pure ternary $CuFeS_2$ NCs. The crystallite size of the phase pure $CuFeS_2$ material can be estimated using Debye-Scherrer analysis, based on the equation

$$D_p = \frac{K\lambda}{\beta\cos\theta},$$

where D_p is the crystallite size, K is the shape factor usually taken close to unity, β (in radian) is the broadening at half maximum or full width at half maximum (FWHM), and θ is the Bragg angle.[30] Here, the value of K is taken 0.94, and wavelength (λ) is 1.54059 Å for Cu K_α lines of the X-ray. The full width at half maxima (β) was calculated using OriginPro software (OriginLab, Northampton, MA) for the (112) Miller index

Table I. Crystallite sizes (Scherrer-analysis) of $CuFeS_2$ NCs synthesized with different growth durations.

S.No.	Growth time	Crystallite size (D_p) (nm)
1.	5 min	9
2.	10 min	12
3.	15 min	22
4.	30 min	26
5.	1 h	34
6.	2 h	39

peaks. An XRD broadening of 0.08° was subtracted from FWHM to calculate the crystallite size of the $CuFeS_2$ chalcopyrite NCs. This XRD instrumental broadening for corresponding "2θ" was obtained from JADE software from a calibration profile of standard NIST 640e silicon sample. The crystallite sizes of $CuFeS_2$ NCs obtained from Scherrer analyses is presented in Table I. The calculated value is rounded to the closest whole number in nanometer. These results indicate that the crystallite size of the $CuFeS_2$ NCs depends upon the growth durations after injecting the S precursor during the synthesis.

Figure 2 shows SEM results of as-synthesized $CuFeS_2$ chalcopyrite NCs with growth times of 15 min, 30 min, 1 h, and 2 h. The as-synthesized NCs have irregular shapes, unlike most preparations of pyrite FeS_2 NCs, which when synthesized by a similar procedure shows a consistent cubic shape.[14] Here, the particle sizes observed by SEM are larger than the crystallite size estimated by Debye-Scherrer equation indicating the crystallites agglomerate to form larger particles. Based on the measured diffractograms, these NC samples all possess tetragonal crystal structure in the chalcopyrite phase. The longest growth time correlates with larger $CuFeS_2$ crystallite size[8] with visual evidence of tetragonal shapes with larger facets and longer clean edges as seen in Fig. 2. More SEM results with different resolutions are shown in Fig. S2 (in SI). As shown in Fig. 2, 15 min growth time yields smaller and less fully crystalline NCs than do the longer growth times. However, for 240 °C injection and 270 °C growth temperatures, the phase and compositional purity of the product NCs are not affected over this range of growth time from 15 min to 2 h (Fig. S1). The $CuFeS_2$ NCs synthesized here have relatively larger particle sizes compared to the previous reports. For example, Wang et al. have reported the spherical and pyramidal shaped tetragonal crystal structure $CuFeS_2$ chalcopyrite NCs with average sizes of 12 and 30 nm, respectively.[11] Liang et al. have synthesized smaller $CuFeS_2$ NCs with 6.6 nm average size.[3]

Further, to compare the surface morphology and size of the particles observed in SEM images, STEM images of $CuFeS_2$ NCs prepared for two growth time (30 min and 1 h) were also obtained as shown in Fig. S3. The size of the $CuFeS_2$ NCs prepared for a growth time of 30 min is ~20 nm, slightly

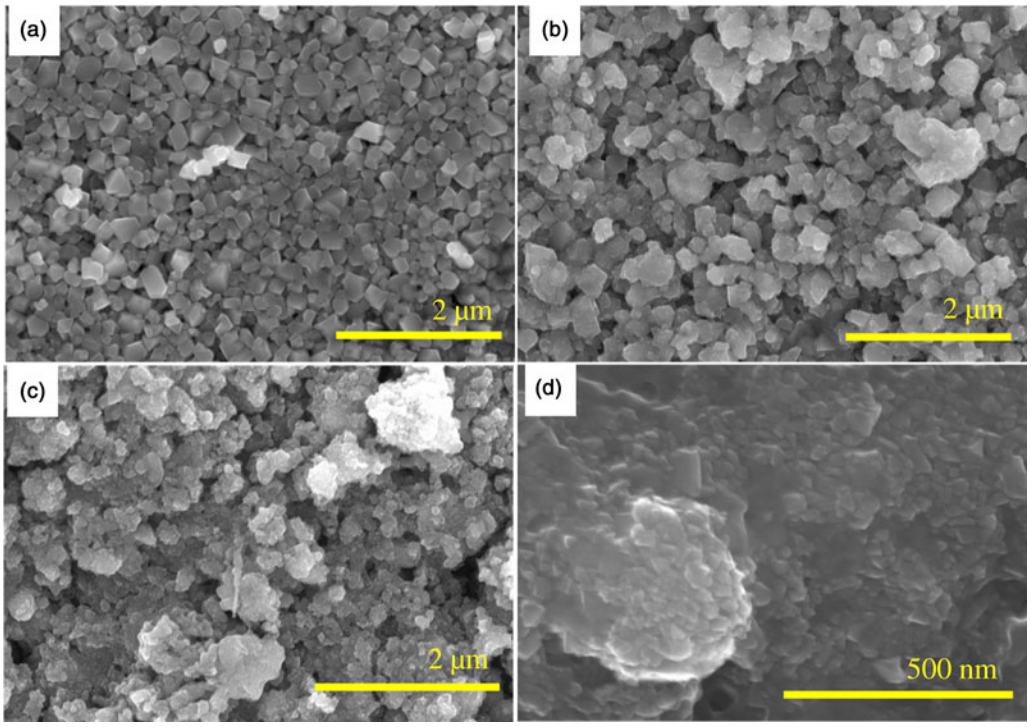

Figure 2. Scanning electron micrographs of as-synthesized $CuFeS_2$ chalcopyrite NCs with different growth durations (a) 2 h, (b)1 h, (c) 30 min, and (d) 15 min.

smaller than crystallite sizes obtained from Scherrer analysis. Similarly, the average particle size prepared for 1 h growth time is ~50 nm. EDS and elemental mapping were used to determine the chemical composition as a function of growth time. EDS confirmed the presence of Cu, Fe, and S atoms in the NCs. The atomic percentages of different elements as a function of growth time are shown in Table SI. Elemental mapping for the 1 h grown $CuFeS_2$ NC sample is shown in Fig. S4 and corresponding EDS data as a function of growth duration are in Fig. S5. From these results, $CuFeS_2$ NCs are found to have slightly higher Cu concentration compared with Fe. The atomic ratio of Cu:Fe:S is close to 1:1:2 indicating tetragonal $CuFeS_2$ chalcopyrite NCs (Table SI), and it agrees with previous results (Cu:Fe:S = 1:0.83:1.96) reported by Wu et al.[5] In case of 30 min growth sample (T_i = 240 °C, T_g = 270 °C), the number of Cu and Fe atoms are relatively close (Table SI) to each other although all the NCs were prepared using an identical procedure except the growth time.

Unpolarized transmittance and Raman spectroscopy

Unpolarized transmittance spectra of $CuFeS_2$ NCs were measured using a Lambda 1050 spectrophotometer (Perkin Elmer) in chloroform solution, referenced to the neat solvent, in a 2 mm path length cuvette. Figure 3 shows the absorbance spectra determined by using Beer's Law from the unpolarized transmittance spectra collected from 250 to 1650 nm. The spectra were recorded for NC samples having growth times of 1, 5, 10, 15, 30, and 60 min, respectively. A strong absorption peak ~465 nm was observed for the NCs with growth time of 1 min. The UV-Vis spectra show that the absorption peak wavelength slightly increases with increasing growth time. The NCs grown for 30 min have the absorption peak at 490 nm, but 60 min grown NCs do not show this absorption peak. The absorption feature observed at ~490 nm matches closely with previous reports.[5,6,13] A typical absorption spectrum in the range of 400–2500 nm for 1 h grown $CuFeS_2$ NCs solution is shown in Fig. S6 (SI).

Based on the literature, other materials showing absorption peaks in the 290 to 600 nm regions include CuO with an absorption peak at ~290 nm and CuS with an absorption peak at ~430 nm.[31] Further, $Cu_{2-x}S$ nanoparticles (NPs) show a broad IR absorption feature ascribed to a localized surface plasmon resonance.[29] FeO NPs reported by Liu et al. do not have any absorption peaks in the region <600 nm.[32] Just prior to initiating the $CuFeS_2$ synthesis, reactants were evacuated at 120 °C to remove oxygen and water, and the synthesis was carried out in a high purity nitrogen environment to avoid any reaction with atmospheric oxygen. Further, the XRD patterns of $CuFeS_2$ NCs grown for longer than 10 min at temperature 270 °C is phase-pure tetragonal $CuFeS_2$ NCs with no other observable impurities (Fig. S1). However, the NCs

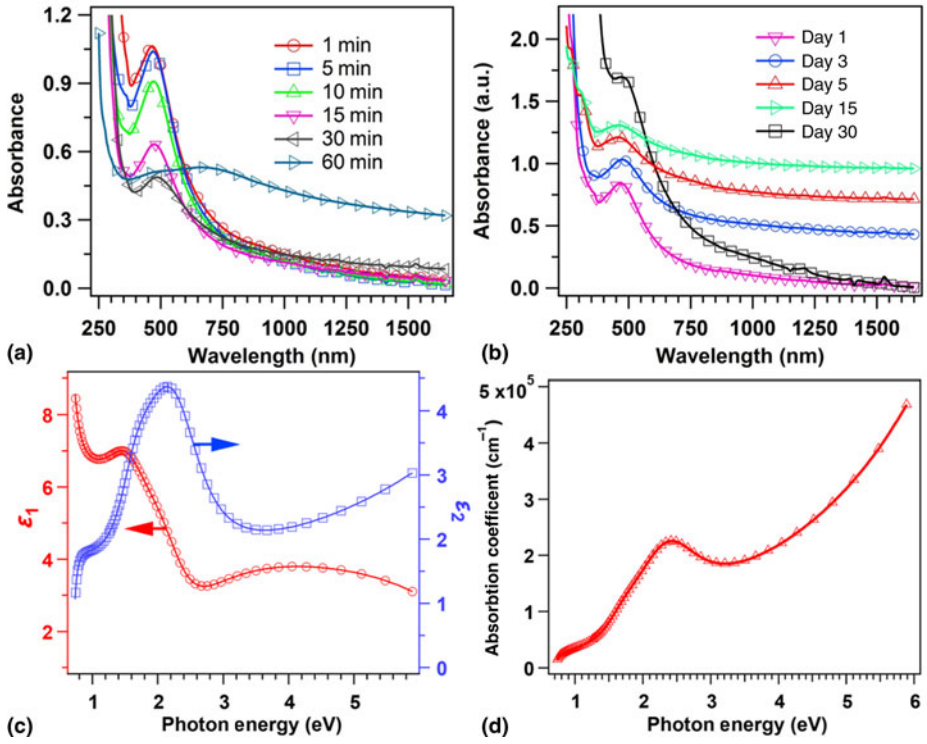

Figure 3. Optical properties of $CuFeS_2$ nanocrystals (a) absorbance spectra of as-synthesized $CuFeS_2$ NCs dispersed in chloroform in 2 mm optical path length cuvette as a function of growth time (b) stability test in 30 days (c) real and imaginary dielectric constants (ε) with photon energy for 15 min grown NCs at 270 °C, and (d) absorption coefficient (α) evaluated from spectra in k using spectroscopic ellipsometry.

grown for 5 min at the same temperature may include traces of CuS as evident from the diffraction pattern (Fig. S1) at ~27.7° (vide supra). Wiltrout et al. have reported an absorption peak at ~600 nm arising from bornite (Cu_5FeS_4) NPs, but our XRD studies do not show the presence of Cu_5FeS_4 or any other cubic phases.[33] Thus, we assign the absorption peaks in the 465–490 nm range to pure tetragonal $CuFeS_2$ NCs.

Previously, many authors have reported blue shifting of the band gap of the $CuFeS_2$ NCs compared with its bulk counterpart (~0.6 eV), which they attributed to quantum confinement.[3,5,11] Some authors have correlated an absorption feature observed in chalcopyrite NCs at ~498 nm with a possible surface plasmon resonance.[13] Our spectra show a very narrow red shift (~25 nm) when increasing the NC growth time from 1 min to 30 min at 270 °C. The small red shift observed from 465 to 490 nm may be attributed to the weak quantum confinement or the surface effects of $CuFeS_2$ NCs. The change in band gap of these $CuFeS_2$ NCs with growth time is quite different from other quantum confined NCs such as PbS and CdSe. For example, in the case of PbS quantum dots, the absorption peaks shift rapidly from 970 to 1740 nm (1.28 to 0.71 eV) within the growth time of 1–20 min.[34] The band gap of $CuFeS_2$ NCs cannot be tuned by quantum confinement as widely as that of PbS, since the Bohr exciton radius of $CuFeS_2$ NCs should be similar to that of iron pyrite (1.3 nm)[35] and $CuInS_2$ (4.1 nm)[36], but much smaller than PbS (18 nm)[34]. Since the size of the NCs prepared here are larger than the Bohr exciton radius, strong quantum confinement is neither present nor expected.

The electronic structure for bulk chalcopyrite $CuFeS_2$ has been discussed in available literature.[1,23,24,37] The theoretical calculation shows an indirect band gap of 0.63 eV in between VB and IB-I, and the width of IB band is ~1.10 eV.[6] The small band gap of this bulk chalcopyrite arises due to the electronic transition from VB to IB-I predominantly formed by empty Fe 3d orbitals.[24] The suppression of the absorption feature at ~490 nm for larger NCs fabricated at longer growth time may be due to several reasons including scattering by larger particles, defect states or unpassivated dangling bonds on the surface. Further study will be required to understand the influence of $CuFeS_2$ NC size on defect densities and optical properties. Thus, based on this observation, we conclude that the absorption peaks observed in the spectral range of 465–490 nm (2.66 to 2.53 eV) is not due to the quantum confinement effect; instead it arises from an electronic transition from the VB to the IB-II located within the fundamental band gap (3.1 eV)[24] of $CuFeS_2$ NCs which is the characteristics of $CuFeS_2$ materials. Further, the complex optical properties of these $CuFeS_2$ NCs were studied using spectroscopic ellipsometry technique in the range of 0.735 to 5.887 eV which is discussed in the section "Optical Properties Using Spectroscopic Ellipsometry".

The stability of these colloidal $CuFeS_2$ NCs is tracked via absorbance spectra of NCs solution dispersed in chloroform, kept in a vial (solution and in air) and stored in ambient environment. The absorbance spectra for 15 min grown $CuFeS_2$ NCs measured at different intervals of time (day 1, day 3 etc) after preparation is presented in Fig. 3(b). From day 1 to day 30, no significant changes in the absorption feature of these NCs are observed indicating that these NCs are quite stable in ambient conditions. The NCs concentration in solution may be slightly different in each measurement giving rise to decreased peak intensity, and some agglomeration of NCs is expected over the time. Further, the XRD pattern of $CuFeS_2$ NC films stored in an ambient environment and measured after 30 days of preparation matches with the standard XRD pattern of chalcopyrite $CuFeS_2$ (#PDF 98-000-0156) with no other phases materials (Fig. S7). The XRD patterns along with consistently shaped absorbance spectra indicate that these NCs are stable in air.

The active vibrational modes present in the NCs were determined from Raman spectroscopy measurement using a HeNe laser of 632.8 nm wavelength (Fig. S8). The measured Raman spectrum matches quite closely with the spectra reported previously for the bulk $CuFeS_2$ excited with a 514.5 nm laser.[38] For as-synthesized NCs, active peaks at positions 290, 351, and 470 cm^{-1} were observed. Based on the literature of similar observations[12,38], the active peaks at 290, 351, and 470 cm^{-1} are assigned to be A_1, B_1, and E phonon modes. The active peak at 290 cm^{-1} is the strongest as evident from the spectrum for the A_1 modes of vibration. Thus, based on XRD pattern, elemental composition, and Raman active modes of vibration, chalcopyrite $CuFeS_2$ NCs synthesized here are phase pure with tetragonal crystal structure.

Optical properties using spectroscopic ellipsometry

Complex optical properties of the $CuFeS_2$ NC thin film can be described by the complex dielectric function, $\varepsilon(E) = \varepsilon_1(E) + i\varepsilon_2(E)$, or the complex refractive index, $N(E) = n(E) + ik(E) = \varepsilon^{1/2}(E)$, spectra as obtained from spectroscopic ellipsometry measurement and analysis (see SI) where ε_1 = real part of dielectric constant, ε_2=imaginary part of dielectric constant, n = refractive index, k = extinction coefficient, and E = photon energy, respectively. These complex quantities, $\varepsilon(E)$ and $N(E)$, are also called optical constant which determines reflection and absorption of media when light travel. The spectra in ε and the structural parameters, the surface roughness, and NC film thickness are extracted by fitting the experimental ellipsometric spectra to a model consisting of semi-infinite soda lime glass substrate/NC film/surface layer/air ambient. Spectra in ε for the NC film are parameterized by using multiple critical point parabolic band (CPPB) oscillators[39] each of which is described by

$$\varepsilon(E) = \varepsilon_\infty + \sum_n A_n e^{i\varphi_n}\left(\frac{\Gamma_n}{2E_n - 2E - i\Gamma_n}\right)^{\mu_n}$$

This CPPB oscillator model describes the optical constant of the material at the interband critical point (CP). For each CPPB

oscillator, A_n is the amplitude, Γ_n is the broadening, E_n is the critical point energy, μ_n is the exponent, and ϕ_n is the phase projection factor. Excitonic transitions ($\mu_n = 1$) are assumed similar to those used to describe FeS_2 NCs.[39] To account the dispersion outside our measured spectral range a constant additive term to ε_1 denoted by ε_∞ is also included in parameterization. Spectra in ε describing the surface layer of film are modeled using the Bruggeman effective medium approximation[40] consisting of 0.834 ± 0.004 of the volume fraction to be identical to $CuFeS_2$ NCs layer and the remainder void. In addition to the parameters describing spectra in ε, the NCs film thickness (d_b) and surface layer thicknesses (d_s) are also free parameters in the least squares regression fit. The thicknesses as obtained from the parametric model are $d_b = 962 \pm 4$ nm and $d_s = 251 \pm 2$ nm, respectively. The surface layer can be interpreted as a combination of roughness and lower packing density of NCs near the top of the deposited film. The high value of d_s corresponds to the sample non-uniformity of the film near the surface and/or grading in NCs packing density. The fitted values with error bars are reported in Table SII (SI) with mean square error (σ) = 3.5×10^{-3}. There are three interband transitions represented by the resonance energies of CPPB oscillators at 0.652 ± 0.003, 1.54 ± 0.03, and 2.29 ± 0.01 eV, respectively, along with an additional oscillator needed to account for higher energy transitions outside the measured spectral range. Spectra in ε and N are shown in Fig. 3(c) and Fig. S9 (in SI), respectively. From spectra in N, the absorption coefficient, $\alpha = 4\pi k(\lambda)/\lambda$ is evaluated which is shown in Fig. 3(d). The CP near 0.65 eV corresponds to the difference in energy between the VB and IB-I which is consistent with the absorption edge at 0.6 eV reported by Teranishi et al.[41] Origin of CPs near 1.54 and 2.29 eV are may be due to transition from VB to Fe 3d orbitals. The transition energies for single crystal $CuFeS_2$ according to Oguchi et al.[23] are 1.0 and 2.1 eV, respectively. In comparison, our CPs are blue-shifted relative to a single crystal. The nature of both spectra in ε and α are similar to that of single crystal $CuFeS_2$[23] but with features lower in magnitude. The critical point energies of these NCs are also red-shifted relative to iron pyrite NCs.[39]

Electronic and Hole Transport Properties

The electronic properties of a material determine the possible application of the material in the opto-electronic devices. The average sheet-resistance of the solution-processed $CuFeS_2$ NC thin films is $7.3\ (\pm 3.7) \times 10^4\ \Omega\,\square^{-1}$ as provided by 4-point probe measurement with an average resistivity of 0.16 (±0.06) Ω cm. Also, these NC films have p-type conductivity as determined by thermal-probe measurement. The $CuFeS_2$ NPs synthesized previously by Liang et al. also shows p-type conductivity with a resistivity of 1.21 Ω cm, and carrier concentration of the order 10^{18} cm^{-3}.[3] In our case, the lower resistivity may be due to the larger particle size of $CuFeS_2$ NCs compared with Liang et al. (6.4 nm). Previously, solution-processed FeS_2 NCs, synthesized by hot-injection route, with resistivity ~10–20 Ω cm and carrier concentration ~10^{18} cm^{-3} have been applied as low barrier interface layer in CdTe and PKSCs.[17,18] Here, these $CuFeS_2$ NC films have lower resistivity compared with FeS_2 NC films and comparable carrier concentration, and hence we

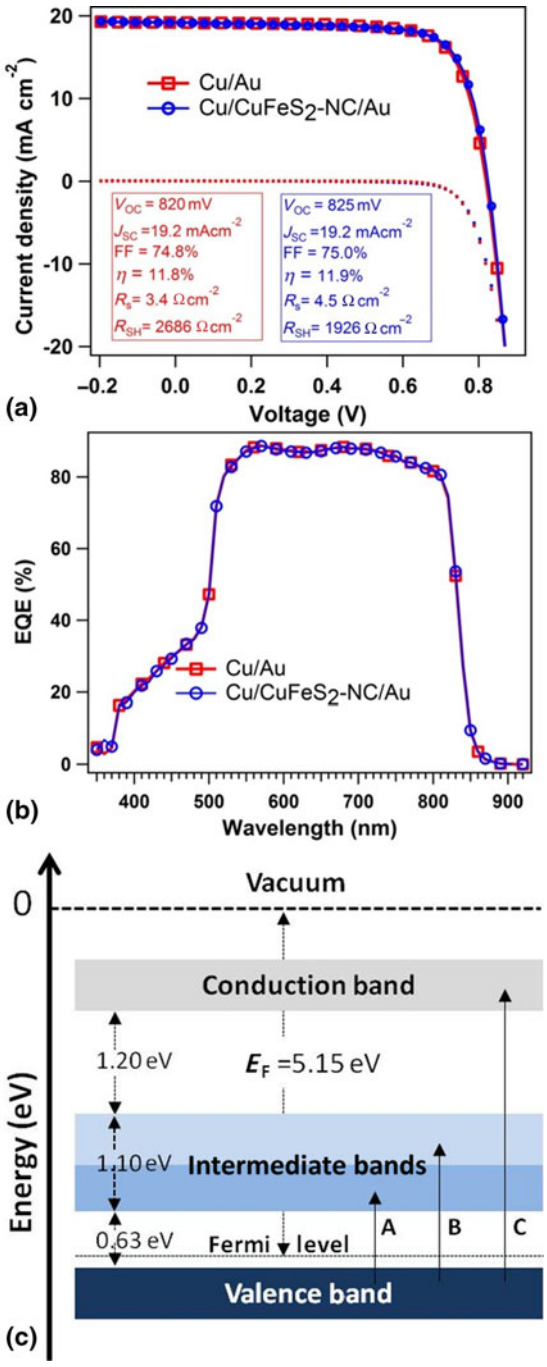

Figure 4. Performance characteristics of the best CdTe devices attained with and without the $CuFeS_2$ NC hole transport layer (a) current-density versus voltage (*J-V*) curves and (b) external quantum efficiency (*EQE*) spectra, and (c) schematic diagram for an electronic structure of bulk chalcopyrite ($CuFeS_2$) materials.

were interested to study the hole transport properties of these materials in CdTe solar cells.

Figure 4 displays the device characteristics of the CdS/CdTe solar cells with two back contacts: Cu/Au and Cu/$CuFeS_2$-NC/Au. The $CuFeS_2$ layer of thickness ~1 μm was prepared using a NCs with growth time of 2 h at 270 °C. A schematic device structure is shown in Fig. S10 (SI). *J-V* characteristics measured under simulated AM1.5G irradiance for best devices are shown in Fig. 4(a) for both Cu/Au and Cu/$CuFeS_2$-NC/Au back contacts. A summary of device parameters for 20 CdTe solar cells with Cu/Au and Cu/$CuFeS_2$-NC/Au back contacts is presented in Table SIII. By introducing $CuFeS_2$ as an interface layer, a slight improvement on open-circuit voltage and fill factor was observed in addition to an increased series resistance of the device compared with the standard Cu/Au. The introduction of the $CuFeS_2$ back contact interface layer resulted in an overall power conversion efficiency that was slightly improved than observed for the Cu/Au back contact design. As a recommended standard practice, the current density (J) as determined by *J-V* measurement was verified by EQE measurement [Fig. 4(b)].

Figure 4(c) displays the schematic diagram for an electronic structure of bulk chalcopyrite $CuFeS_2$ materials which have IBs formed mainly due to the Fe 3d orbitals in between the VB and CB. The electronic transitions, A and B in Fig. 4(c), <3.1 eV are due to transitions from VB to the IBs.[23,24] The previous report has assigned the Fermi level at 5.15 eV below the vacuum level for chalcopyrite ($CuFeS_2$) materials.[37] It may require further studies to understand the band offset mismatch in the case of $CuFeS_2$ NC-film and CdTe interface. Using the $CuFeS_2$-NC film as an interface layer, we found a slight improvement in the V_{OC} and FF with respect to Cu/Au back contact, but a slight decrease in J_{SC}. The decrease in J_{SC} is compensated by V_{OC} and FF to yield similar device performance in both cases. The additional effect due to the $CuFeS_2$ interface layer we observed is the increase in the series resistance of the solar cells, and it may require further treatment to increase the conductivity of the NC interface layer. Two possible reasons for the non-ideal interface layer performance of the $CuFeS_2$ NC HTL are (i) the large distribution of particle sizes, and (ii) weak adhesion of the HTL film to CdTe. Currently, we are working to control the NC size distribution, to improve the interface between CdTe and the $CuFeS_2$ NC-film, and to study the hole transport properties of these $CuFeS_2$ NCs in other PV devices. Based on our preliminary results of using $CuFeS_2$ NCs as HTLs in CdTe devices, these NCs may find similar applications in other material systems and device structures.

Conclusions

We have successfully synthesized phase pure and stable chalcopyrite $CuFeS_2$ NCs using a thermal-injection colloidal route. In the synthesis process, the elemental sulfur powder was used as the S source. The nucleation temperature and growth duration of the NCs play critical roles in the synthesis of phase pure and stable ternary $CuFeS_2$ NCs. These NCs possess tetragonal crystal structure in chalcopyrite phase. A strong absorption peak at ~465 nm was observed for 1 min grown NCs, which shifted to 490 nm after 30 min, and it disappeared for 1 h grown $CuFeS_2$ NCs. From spectra in ε, interband transitions are identified at 0.652 ± 0.003, 1.54 ± 0.03, and 2.29 ± 0.01 eV, which are attributed to transitions from the VB to IBs formed by Fe 3d orbitals. The average sheet resistance of $CuFeS_2$ NC films was found to be $7.3\ (\pm 3.7) \times 10^4\ \Omega\,\square^{-1}$ with an average resistivity of 0.16 (±0.06) Ω cm. Our preliminary results demonstrate the potential application of $CuFeS_2$ NC-based thin films as the HTL in thin film solar cells.

Supplementary material

The supplementary material for this article can be found at https://doi.org/10.1557/mrc.2018.117.

Acknowledgments

The authors gratefully acknowledge funding from the US National Science Foundation Sustainable Energy Pathways program for funding under Grant CHE-1230246, the U.S. Air Force Research Laboratory, Space Vehicles Directorate (contract # FA9453-11-C-0253), the Ohio Department of Development Ohio Research Scholar Program Northwest Ohio Innovators in Thin Film Photovoltaics Grant No. TECH 09-025, and startup funds provided by the University of Toledo.

References

1. T. Kambara: Optical Properties of a magnetic semiconductor: chalcopyrite $CuFeS_2$ II. Calculated electronic structures of $CuGaS_2$:Fe and $CuFeS_2$. *J. Phys. Soc. Jpn.* **36**, 1625 (1974).
2. S. Conejeros, P. Alemany, M. Llunell, I.D.P.R. Moreira, V.C. Sánchez, and J. Llanos: Electronic structure and magnetic properties of $CuFeS_2$. *Inorg. Chem.* **54**, 4840 (2015).
3. D. Liang, R. Ma, S. Jiao, G. Pang, and S. Feng: A facile synthetic approach for copper iron sulfide nanocrystals with enhanced thermoelectric performance. *Nanoscale* **4**, 6265 (2012).
4. J. Li, Q. Tan, and J.-F. Li: Synthesis and property evaluation of $CuFeS_{2-x}$ as earth-abundant and environmentally-friendly thermoelectric materials. *J. Alloys. Compd.* **551**, 143 (2013).
5. Y. Wu, B. Zhou, C. Yang, S. Liao, W.-H. Zhang, and C. Li: $CuFeS_2$ colloidal nanocrystals as an efficient electrocatalyst for dye sensitized solar cells. *Chem. Commun.* **52**, 11488 (2016).
6. S. Ghosh, T. Avellini, A. Petrelli, I. Kriegel, R. Gaspari, G. Almeida, G. Bertoni, A. Cavalli, F. Scotognella, T. Pellegrino, and L. Manna: Colloidal $CuFeS_2$ nanocrystals: intermediate Fe d-band leads to high photothermal conversion efficiency. *Chem. Mater.* **28**, 4848 (2016).
7. D. Aldakov, A. Lefrancois, and P. Reiss: Ternary and quaternary metal chalcogenide nanocrystals: synthesis, properties and applications. *J. Mater. Chem. C* **1**, 3756 (2013).
8. M. X. Wang, L. S. Wang, G. H. Yue, X. Wang, P. X. Yan, and D. L. Peng: Single crystal of $CuFeS_2$ nanowires synthesized through solventothermal process. *Mater. Chem. Phys.* **115**, 147 (2009).
9. E. J. Silvester, T. W. Healy, F. Grieser, and B. A. Sexton: Hydrothermal preparation and characterization of optically transparent colloidal chalcopyrite ($CuFeS_2$). *Langmuir* **7**, 19 (1991).
10. S. K. Pradhan, B. Ghosh, and L. K. Samanta: Mechanosynthesis of nanocrystalline chalcopyrite. *Phys. E.* **33**, 144 (2006).
11. Y.-H. A. Wang, N. Bao, and A. Gupta: Shape-controlled synthesis of semiconducting $CuFeS_2$ nanocrystals. *Solid State Sci.* **12**, 387 (2010).

12. P. Kumar, S. Uma, and R. Nagarajan: Precursor driven one pot synthesis of wurtzite and chalcopyrite $CuFeS_2$. *Chem. Commun.* **49**, 7316 (2013).
13. G. Gabka, P. Bujak, J. Z˙ukrowski, D. Zabost, K. Kotwica, K. Malinowska, A. Ostrowski, I. Wielgus, W. Lisowski, and J. W. Sobczak: Non-injection synthesis of monodisperse Cu–Fe–S nanocrystals and their size dependent properties. *Phys. Chem. Chem. Phys.* **18**, 15091 (2016).
14. K. P. Bhandari, P. J. Roland, T. Kinner, Y. Cao, H. Choi, S. Jeong, and R. J. Ellingson: Analysis and characterization of iron pyrite nanocrystals and nanocrystalline thin films derived from bromide anion synthesis. *J. Mater. Chem. A* **3**, 6853 (2015).
15. T. Kinner, K. P. Bhandari, E. Bastola, B. M. Monahan, N. O. Haugen, P. J. Roland, T. P. Bigioni, and R. J. Ellingson: Majority Carrier Type Control of Cobalt Iron Sulfide ($Co_xFe_{1-x}S_2$) Pyrite Nanocrystals. *J. Phys. Chem. C* **120**, 5706 (2016).
16. B. Bhattacharyya and A. Pandey: $CuFeS_2$ quantum dots and highly luminescent $CuFeS_2$ based core/shell structures: synthesis, tunability, and photophysics. *J. Am. Chem. Soc.* **138**, 10207 (2016).
17. K. P. Bhandari, P. Koirala, N. R. Paudel, R. R. Khanal, A. B. Phillips, Y. Yan, R. W. Collins, M. J. Heben, and R. J. Ellingson: Iron pyrite nanocrystal film serves as a copper-free back contact for polycrystalline CdTe thin film solar cells. *Sol. Energy Mater. Sol. Cells* **140**, 108 (2015).
18. A. J. Huckaba, P. Sanghyun, G. Grancini, E. Bastola, C. K. Taek, L. Younghui, K. P. Bhandari, C. Ballif, R. J. Ellingson, and M. K. Nazeeruddin: Exceedingly cheap perovskite solar cells using iron pyrite hole transport materials. *Chemistryselect* **1**, 5316 (2016).
19. E. Bastola, K. P. Bhandari, and R. J. Ellingson: Application of composition controlled nickel-alloyed iron sulfide pyrite nanocrystal thin films as the hole transport layer in cadmium telluride solar cells. *J. Mater. Chem. C* **5**, 4996 (2017).
20. E. Bastola, K. K. Subedi, K. P. Bhandari, and R. J. Ellingson: Solution-processed nanocrystal based thin films as hole transport materials in cadmium telluride photovoltaics. *MRS Adv.* 1 (2018). doi: 10.1557/adv.2018.349.
21. J. L. Freeouf and J. M. Woodall: Schottky barriers: an effective work function model. *Appl. Phys. Lett.* **39**, 727 (1981).
22. J. Jaffe and A. Zunger: Electronic structure of the ternary chalcopyrite semiconductors $CuAlS_2$, $CuGaS_2$, $CuInS_2$, $CuAlSe_2$, $CuGaSe_2$, and $CuInSe_2$. *Phys. Rev. B* **28**, 5822 (1983).
23. T. Oguchi, K. Sato, and T. Teranishi: Optical reflectivity spectrum of a $CuFeS_2$ single crystal. *J. Phys. Soc. Jpn.* **48**, 123 (1980).
24. T. Hamajima, T. Kambara, K. I. Gondaira, and T. Oguchi: Self-consistent electronic structures of magnetic semiconductors by a discrete variational Xα calculation. III. Chalcopyrite $CuFeS_2$. *Phys. Rev. B* **24**, 3349 (1981).
25. E. Janik and R. Triboulet: Ohmic contacts to p-type cadmium telluride and cadmium mercury telluride. *J. Phys. D: Appl. Phys.* **16**, 2333 (1983).
26. E. Bastola, K. P. Bhandari, A. J. Matthews, N. Shrestha, and R. J. Ellingson: Elemental anion thermal injection synthesis of nanocrystalline marcasite iron dichalcogenide $FeSe_2$ and $FeTe_2$. *RSC Adv.* **6**, 69708 (2016).
27. Z. Hosseinpour, A. Alemi, A. A. Khandar, X. Zhao, and Y. Xie: A controlled solvothermal synthesis of CuS hierarchical structures and their natural-light-induced photocatalytic properties. *New J. Chem.* **39**, 5470 (2015).
28. C. Xing, D. Zhang, K. Cao, S. Zhao, X. Wang, H. Qin, J. Liu, Y. Jiang, and L. Meng: In situ growth of FeS microsheet networks with enhanced electrochemical performance for lithium-ion batteries. *J. Mater. Chem. A* **3**, 8742 (2015).
29. P. L. Saldanha, R. Brescia, M. Prato, H. Li, M. Povia, L. Manna, and V. Lesnyak: Generalized one-pot synthesis of copper sulfide, selenide-sulfide, and telluride-sulfide nanoparticles. *Chem. Mater.* **26**, 1442 (2014).
30. J. I. Langford and A. Wilson: Scherrer after sixty years: a survey and some new results in the determination of crystallite size. *J. Appl. Crystallogr.* **11**, 102 (1978).
31. A. El-Trass, H. ElShamy, I. El-Mehasseb, and M. El-Kemary: CuO nanoparticles: synthesis, characterization, optical properties and interaction with amino acids. *Appl. Surf. Sci.* **258**, 2997 (2012).
32. P. Liu, W. Cai and H. Zeng: Fabrication and size-dependent optical properties of FeO nanoparticles induced by laser ablation in a liquid medium. *J. Phys. Chem. C* **112**, 3261 (2008).
33. A. M. Wiltrout, N. J. Freymeyer, T. Machani, D. P. Rossi, and K. E. Plass: Phase-selective synthesis of bornite nanoparticles. *J. Mater. Chem.* **21**, 19286 (2011).
34. I. Moreels, K. Lambert, D. Smeets, D. De Muynck, T. Nollet, J. C. Martins, F. Vanhaecke, A. Vantomme, C. Delerue, G. Allan, and Z. Hens: Size-dependent optical properties of colloidal PbS quantum dots. *Acs Nano* **3**, 3023 (2009).
35. W. Li, M. Doblinger, A. Vaneski, A. L. Rogach, F. Jackel, and J. Feldmann: Pyrite nanocrystals: shape-controlled synthesis and tunable optical properties via reversible self-assembly. *J. Mater. Chem.* **21**, 17946 (2011).
36. S. L. Castro, S. G. Bailey, R. P. Raffaelle, K. K. Banger, and A. F. Hepp: Nanocrystalline chalcopyrite materials ($CuInS_2$ and $CuInSe_2$) via low-temperature pyrolysis of molecular single-source precursors. *Chem. Mater.* **15**, 3142 (2003).
37. Y. Xu and M. A. Schoonen: The absolute energy positions of conduction and valence bands of selected semiconducting minerals. *Am. Mineral.* **85**, 543 (2000).
38. W. Chunrui, X. Shaolin, H. Junqing, and T. Kaibin: Raman, far infrared, and mössbauer spectroscopy of $CuFeS_2$ Nanocrystallites. *Jpn. J. Appl. Phys.* **48**, 023003 (2009).
39. I. Subedi, K. P. Bhandari, R. J. Ellingson, and N. J. Podraza: Near infrared to ultraviolet optical properties of bulk single crystal and nanocrystal thin film iron pyrite. *Nanotechnology* **27**, 295702 (2016).
40. V. D. Bruggeman: Berechnung verschiedener physikalischer Konstanten von heterogenen Substanzen. I. Dielektrizitätskonstanten und Leitfähigkeiten der Mischkörper aus isotropen Substanzen. *Ann. Phys.* **416**, 636 (1935).
41. T. Teranishi and K. Sato: Optical, electrical and magnetic properties of chalcopyrite, $CuFeS_2$. *J. Phys. Colloques* **36**, C3 (1975).